Spatially entangled four-photon states

Alexander J.H. van der Torren
Quantum Optics
Leiden university

August 31, 2011

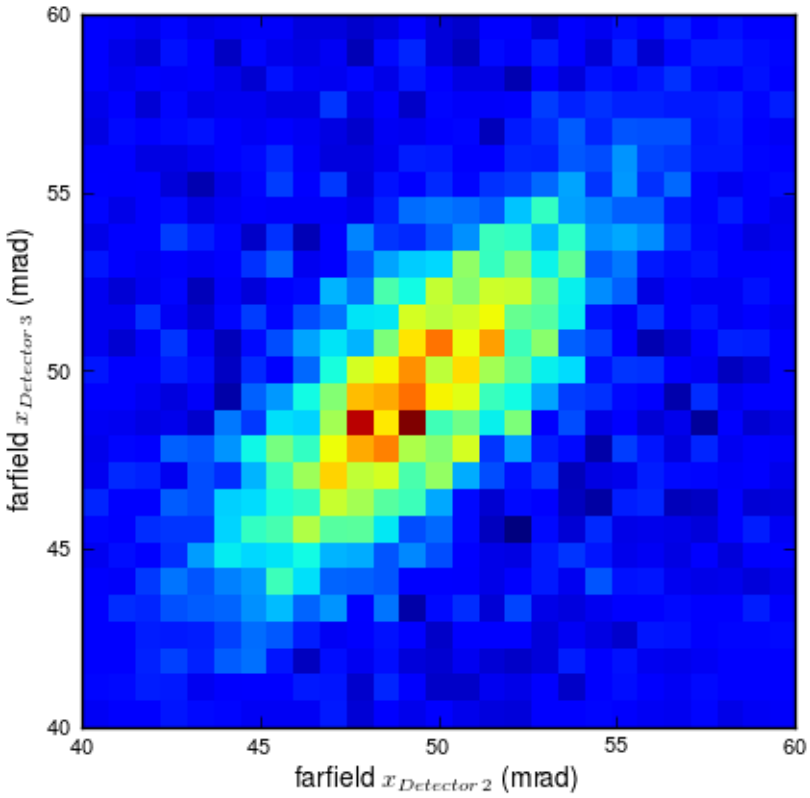

Contents

Chapter 1

General intro

An entangled photon pair consists of two photons that share a non-classical correlation: It is impossible to gain knowledge about a physical parameter by measuring a single particle. However, a measurement on one of the particles immediately dictates the outcome of the measurement on he other particle. Entangled photon pairs play an important role in quantum information where they are used to demonstrate quantum non-locality, quantum teleportation and quantum cryptography. For quantum cryptography single entangled photon pair are enough while quantum computation requires a quantum state of more than two particles that are simultaneously entangled.

In this project we will investigate four-photons states that are simultaneously entangled in the spatial degree of freedom. A similar situation in the time domain has been described theoretically [9] and experimentally [12].

Entangled photon state are commonly created in non-linear crystals by a process called spontaneous parametric down conversion process (SPDC). Most often this process is thought of as creating single pairs of photons using the vacuum state as input. Four photons states can be generated either by the accidental production of two spontaneous pairs or by stimulated emission, where one spontaneously generated pair triggers the emission of a second identical pair. In order to see the effect of generation of a second pair strong pumping is needed and the four photons have to be generated in a well defined time bin [4, 10]. To satisfy the strong pumping and the well defined time bin a pulsed pump is needed.

This thesis describes the observation of stimulated emission of spatially entangled photon states. Chapter 2 describes the process of collinear second harmonic generation in a PPKTP (periodically poled potassium titanyl phosphate) crystal using short pump pulses. Second harmonic generation is linked and compared to the SPDC process in chapter 3. The spatial entanglement of photon pairs generated with a pulsed pump is investigate in chapter 4. In chapter 5 we finally investigate the spatial entanglement of four photon states and the role of the stimulated emission process.

Chapter 2

Collinear second harmonic generation in PPKTP

2.1 Introduction

Second harmonic generation (SHG), or frequency doubling, is a nonlinear process that converts incoming light to light with twice the frequency, or half the wavelength. This process takes place in an appropriately chosen non-centrosymmetric crystal, with a second-order nonlinearity $\chi^{(2)}$. This nonlinearity ensures the generation of a nonlinear polarization P_{NL} with a quadratic response to the electric field of the light $\mathbf{P}_{NL} \propto \chi^{(2)}E^2 \propto \chi^{(2)}e^{i\omega t}e^{i\omega t} = \chi^{(2)}e^{i2\omega t}$. This polarization on its turn generates the electric field at double frequency.

2.2 Phase matching

To generate second harmonic signals efficiently so called phase-matching conditions are necessary. For a phase-matched configuration the second harmonic field generated over the length of the crystal interferes constructively. In order to fulfill this condition the wave vector of the pump field has to be equal to the sum of the wave vectors of the generated fields $\Delta k = 2k_p - k_s = 0$[1]. Here k_p and k_s are the wave vector of the pump and generated field respectively. In isotropic materials with a monochromatic

pump field this phase-matching condition is equivalent to $n(\omega) = n(2\omega)$ for the refractive index of the material. This condition is generally not satisfied due to index dispersion of the material, typical leading to $n(\omega) < n(2\omega)$. To create a phase-matched interaction one can use, among others, angle tuning of a birefringent nonlinear crystal or quasi-phase-matching in a periodically poled nonlinear crystal. In this project I will use quasi phase-matching.

For quasi-phase-matching, a ferroelectric material is produced in such a way that one of the axes is periodically inverted as function of position. This inversion will cause a periodic flip of the sign of the nonlinear coefficient and consequently a periodic change in the sign of the nonlinear polarization. After each half a coherence length, defined via $L_{coh} = \frac{2}{\Delta k}$, the phase of the dipoles is reversed, and the nonlinear effect will constructively interfere over the entire length of the crystal. The periodically poling of the crystal results in an extra factor in the phase-match function that will result in

$$\Delta k = 2k_p - k_s - k_m = 0 \tag{2.1}$$

with $k_m = \frac{2\pi m}{\Lambda}$ where Λ is the poling period[1] and m is an integer.

The intensity of the SHG light is then given by [1]

$$I \propto I_p^2 L^2 \text{sinc}^2(\frac{1}{2} L\Delta k), \tag{2.2}$$

where I_p is the intensity of the pump and $\text{sinc}(x) \equiv \frac{\sin x}{x}$.

2.3 Pulsed vs continuous wave second harmonic generation

The efficiency of SHG is proportional to the power of the pump squared (equation 2.2). This will result in a much higher second harmonic power for a pulsed laser compared to a continuous pump laser. On the other hand when the pulse length Δt is small the Fourier related frequency bandwidth $\Delta\omega$ is large as $\Delta\omega \cdot \Delta t \geq 1$. This finite bandwidth will give rise to SHG at multiple frequencies, but also allows for the process of sum frequency generation (SFG).

We approximate the shape of the pulsed pump laser, in the frequency and time domain, by a Gaussian. By integrating all contributions to the second harmonic we obtain the second harmonic intensity

$$I \propto I_p^2 L^2 \frac{\tau}{\sqrt{8\ln 2\pi}} \int\int d\omega_{p1} d\omega_{p2} \exp \frac{-((\omega_{p1}+\omega_{p2})-2\omega_0)^2\tau^2}{8\ln 2} \mathrm{sinc}^2(\frac{1}{2}L\Delta k) \tag{2.3}$$

as described in reference [8]. With τ the pulse length of the laser, $\omega_{p1,2}$ the frequencies of the pump photons and ω_0 the central pump frequency. Note that Δk depends on the frequencies $\omega_{p1,2}$. In the cw limit, i.e. τ to infinity, the Gaussian reduces to a delta function and we obtain the result given by equation 2.2.

For pulsed lasers, the finite spectral bandwidth requires us to consider the frequency dependence of $n(\omega)$ and $n(2\omega)$. In general, this group velocity of the signal and pump beam will not be the same in a nonlinear crystal. This difference in group velocity will lead to the effect that the pump and signal beam will not overlap anymore after propagating a distance L_{gvw} in the crystal. This group velocity walk off length is given by[7]

$$L_{gvw} = \tau_p \left(\frac{1}{v_{gs}} - \frac{1}{v_{gp}} \right)^{-1}. \tag{2.4}$$

Here τ_p is the pulse length of the pump and v_{gp} and v_{gs} are the group velocities of the pump and the second harmonic beam respectively. The group velocity is given by $v_g = \frac{d\omega}{dk} = \left(\frac{dk}{d\omega}\right)^{-1} \approx c\left(n + \omega\frac{dn}{d\omega}\right)^{-1}$. This length L_{gvw} is typically a few mm by pump pulses with a duration in the order of picoseconds.

For many crystals a judicious choice of signal, idler wavelength and poling period can be made where the group velocity is matched ($\frac{1}{v_{gs}} - \frac{1}{v_{gp}} = 0$) as well as the phase-match function 2.1. This results in an infinity long group velocity walk off length. Group velocity matching possibilities for PPKTP can be found in [5, 7]. For this report we want the signal and idler wavelength to be equal and around 800 nm. At this wavelengths group velocity matching is not possible.

To calculate the group velocity walk off for our setup we first calculate the group velocities from the Sellmeier equations for the refractive index. The Sellmeier functions for PPKTP are given in reference [3] and the pulse time

of the laser is specified by the factory as 2 ps. With this values equation 2.4 results in $L_{gvw} = 5.4$ mm. Here the polarization of the light is vertical to vertical, the ordinary axes of the crystal.

An alternative way is to write it as frequency spread instead of a walk-off length.

$$A \sim \text{sinc}\left(\pi \frac{(\omega - \omega)}{\Delta\omega_{SHG}}\right) \tag{2.5}$$

with

$$\Delta\omega_{SHG} = \frac{2}{L\pi}\left(\frac{1}{v_{gs}} - \frac{1}{v_{gp}}\right)^{-1} = 1.02 \cdot 10^{12}\text{s}^{-1}, \tag{2.6}$$

which corresponds to $\Delta\lambda = 0.37$ nm at $\lambda = 826$ nm.

2.4 Results

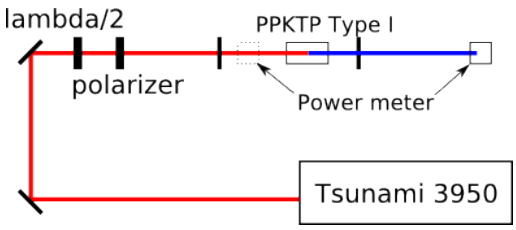

Figure 2.1: *Second harmonic generation setup. The PPKTP Type I crystal is 2 mm long and has a poling period of $\Lambda = 3.675$ μm. The $\frac{\lambda}{2}$-plate and the polarizer are used to tune the power. The red power is measured by placing a power meter in the beam at the place of the dotted box. The SHG power is measured at the end with a power meter.*

Figure 2.1 shows the setup used to generate and measure second harmonic from a Ti:sapphire laser operating at a wavelength of 826 nm. The laser can be operated either as a cw-laser or as a pulsed laser with pulses of length $\tau = 2$ ps by switching on or off the mode-locking. The second harmonic is generated in a 2 mm long PPKTP crystal with a poling period $\Lambda = 3.675$ μm. This 2 mm crystal is safe from the group velocity walk off limit $L_{gvw} = 5.4$ mm calculated in the previous section. We use a Peltier element together with a PID controller to tune the temperature from 10 °C to 90 °C. The combination of $\lambda/2$-plate and polarizer is used to vary the pump power. A power meter

placed just in front of the crystal is used to measure the average power of the pump.

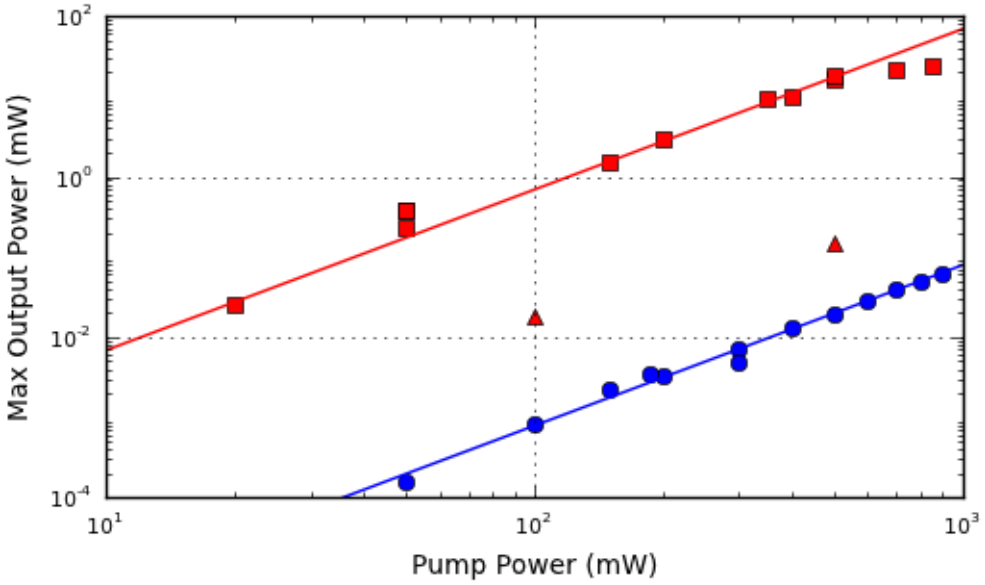

Figure 2.2: *Log-log plot of the measured output power at optimal phase-matching temperature as a function of input power. The squares are for a pulsed pump and the circles for cw pump. The triangles are measurements where the pulsed pump laser is not properly mode-locked. The lines though the data represents a quadratic dependence.*

The measured SH output power as a function of pump power is plotted in figure 2.2 on a log-log scale. Data are shown for pulsed (red squares) and cw-pump (blue circles) and are compared to a quadratic power dependence indicated by the lines though the data. For both the pulsed and continuous pump the output power depends quadratic on the input power. The pulsed pump is expected to give a factor $\frac{1}{\tau f}$ higher output power. Here τ is the pulse duration en f the repetition rate of the laser. For the factory specification values of the laser this would be a factor 6000. The measurements show nearly a factor 10^3 difference in efficiency. This lower efficiency difference could be caused by a not fourier limited pulse and a longer pulse duration.

Figure 2.3 shows the SH power as a function of temperature of the crystal for cw (blue circles) and pulsed (red squares) pump. The solid lines are fits

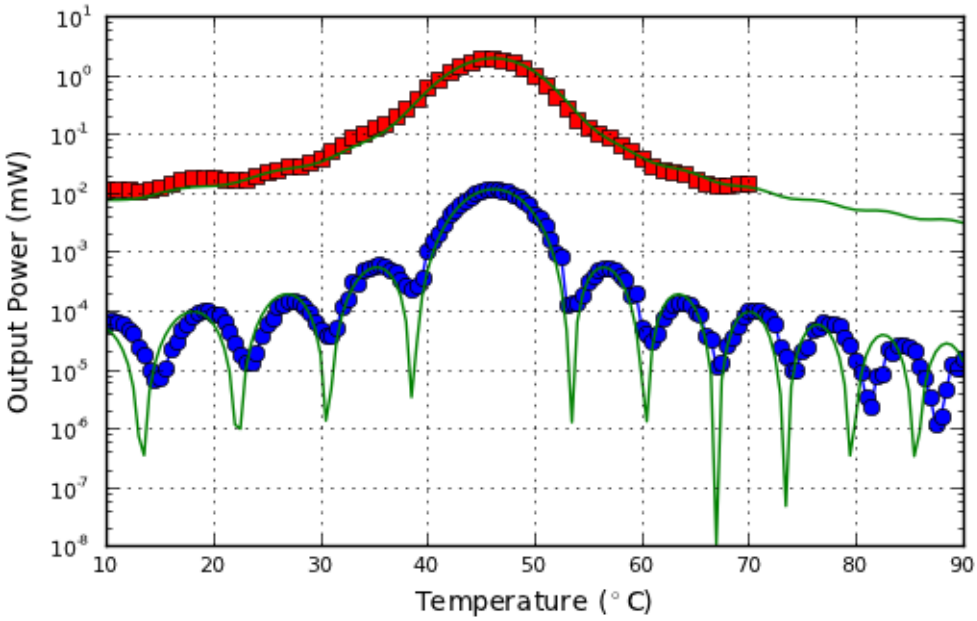

Figure 2.3: *Measured second harmonic in a 2 mm PPKTP crystal as function of crystal temperature. Data are shown for a cw pump (blue circles) and a pulsed pump (red squares) at a pump wavelength of 826.4 nm. The lines through the data are fits using equations 2.2 and 2.3 respectively.*

to the data using equation 2.2 and equation 2.3 respectively. To this end we use the temperature dependent phase-mismatch $\Delta k(T)$, which is easily derived from the temperature dependence of the refractive index $n(T) = n_0 + c_1 T + c_2 T^2$ reported in literature [2, 11]. To avoid the integral of equation 2.3, the integral is approximated by a summation over the signal and idler wavelengths. The summation limits are chosen to be 823.9 nm till 828.9 nm, with steps of 0.1 nm. This summation limits are much wider than the width of the Gaussian pump pulse $\Delta\lambda_p = 0.6$ nm. To be able to fit the top of the sinc for both the cw and pulsed pump an extra phase had to be added into the sinc resulting into $\mathrm{sinc}^2(\frac{1}{2}L\Delta k + \phi)$. This is probably due to the fact measured temperature is not exact and discrepancy in literature values of the refractive index of PPKTP. To compare the width of the cw and pulsed peak, both peaks are fitted with a Gaussian to calculate the ratio of there FWHM. The pulsed phase-match function is a factor 1.3 wider than the cw pump SH phase-match function.

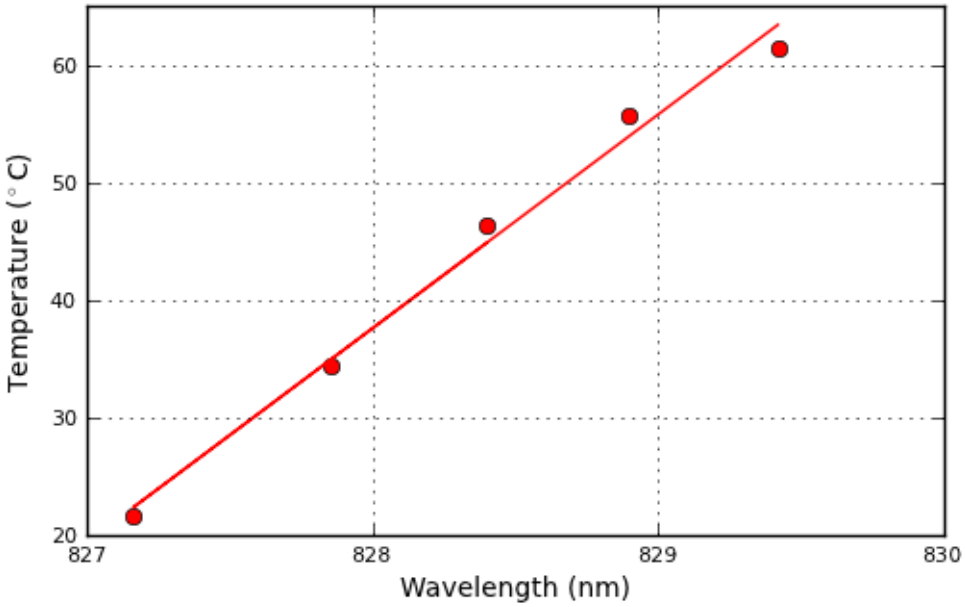

Figure 2.4: *Optimal phase-matching temperature as a function of pump wavelength. The line through the data is a linear fit with a slope of* $18.1 \pm 3.3\ ^\circ C/nm$.

Based on the change of refractive index with temperature we expect a shift in optimal temperature with pump wavelength. To investigate this in more detail we tuned the laser wavelength and recorded the phase-match curve as function of temperature as above. Figure 2.4 shows the optimal phase-match temperature as a function of pump wavelength. The line through the data is a linear fit with a slope of $18.1 \pm 3.3\ ^\circ$/nm.

During our experiments we found that the temperature where maximum SH power is generated depends on pump power. The measured power dependence is shown in figure 2.5 for CW (blue circles) and pulsed (red squares) laser operation. The linear change in the optimal temperature for a cw pump (blue circles) is consistent with heating of the light. This heating is not measured by the temperature sensor because it is installed in the holder under the crystal and does not measure the actual crystal temperature at the position of the laser beam. In contrast, the temperature for optimal power with a pulsed pump (red squares) can not be explained by a heating argument only, because we expect the heating effect to depend on the time average power

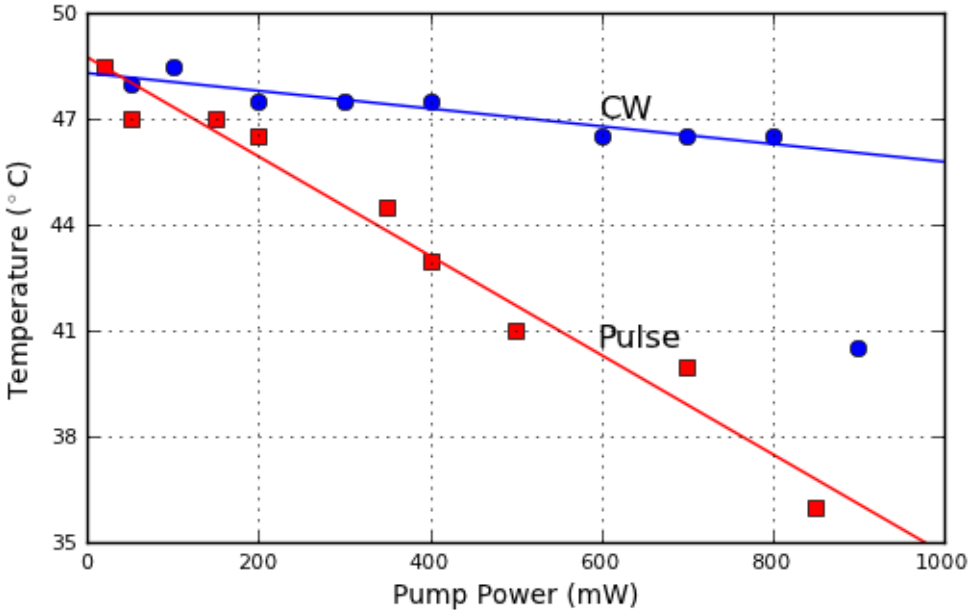

Figure 2.5: *Measured optimal phase-match temperature as a function of pump power for cw (blue circles) and pulsed laser (red squares). The decrease in set temperature with pump power is a factor 5.6 larger for pulsed laser.*

which is equal for the pulsed and cw pump beam. Therefore, we speculate that other non-linear effects, e.g. Kerr effect, are important.

Chapter 3

Angular distribution of SPDC light in PPKTP for a pulsed pump

3.1 Introduction

Spontaneous parametric down conversion (SPDC) is the inverse process of sum frequency generation. In this process a pump photon splits spontaneously into two photons, in such a way that the total energy is conserved. In this process only the pump photon has a well-defined direction and frequency. This gives freedom to the two photons generated via SPDC to exit at different angles and frequencies as long as they obey energy conservation and fulfill the phase-matching condition. For SPDC the phase-matching condition dictates that the wave vectors of the two generated photons must add up to the wave vector of the pump photon.

3.2 Experimental setup

To investigate the angular distribution of the light generated by degenerate SPDC, we place a camera in the far-field behind the crystal as depicted in figure 3.1. A GaP filter blocks the pump light, while a bandpass filter selects only the degenerate frequency that is exactly half of the pump frequency,

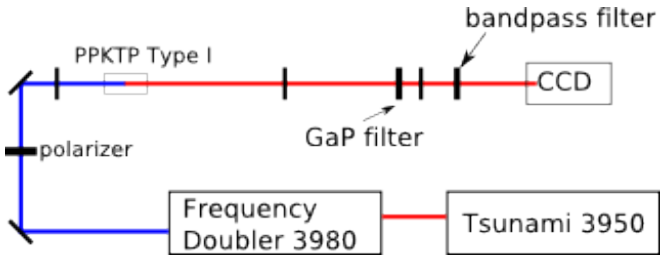

Figure 3.1: *Experimental setup used to record the far-field of 826nm light produced by parametric down conversion of 413nm laser pulses. The pump beam is focused into the crystal with a $f = 10$ cm lens. The output from the PPKTP crystal is collected by a lens with $f = 10$ cm, and imaged on a CCD camera with a $f = 2.5$ cm lens filtered by a GaP wafer and a 1 nm bandpass filter at a center frequency of 826.34 nm. All the lenses are put as good as possible at there focal distances, so that the pump pulse, that we consider to be a parallel beam, makes a far-field image on the CCD.*

ensuring that the two generated photons have the same frequency. This bandpass filter is centered at 826.34nm and has a fill-width-half-maximum (FWHM) of 1 nm.

Figure 3.2 shows the recorded far-field images for a crystal temperature of 20, 30 and 40 °C. The position on the CCD was converted to a far-field angle using the focal distance $f = 25$ mm of the lens. At increased temperature the exit angle of the generated photons is observed to decrease, to compensate for the change in the phase-matching condition. The invariance of the type-I SPDC process for rotation around the z-axis results in a ring of photons collected in the far-field. Collinear SPDC is achieved for a set temperature of about 40 °C. This temperature can be compared directly to the optimal phase-matching temperature for collinear SHG described in chapter 2.

Comparing this results with a continuous pump is not possible in our setup due to the to low pump power with a cw-pump. To generate our 413 nm pump we use the SHG process to convert our 826 nm pump. This process is very inefficient with a cw-pump.

To describe the SPDC process quantitatively we will assume a plane wave for the pump field and a collinear setup. The interaction Hamiltonian is then

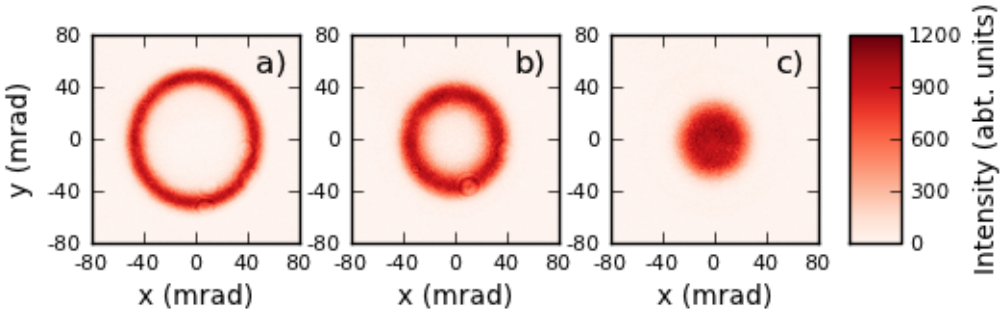

Figure 3.2: *Far-field images of the angular distribution of SPDC light generated from a 2 mm PPKTP crystal. The CCD images are recorded with a 1 nm bandpass filter at crystal temperatures of: a)* 20 °*C, b)* 30 °*C and c)* 40 °*C.*

given by

$$H_I(t) = \int d\vec{k}_1 \int d\vec{k}_2 \int d\vec{r} C e^{i(\vec{k}_p - \vec{k}_1 - \vec{k}_2)\vec{r}} e^{-i(\omega_p - \omega_1 - \omega_2)t} a^\dagger(\vec{k}_1) a^\dagger(\vec{k}_2) + \text{h.c.} \tag{3.1}$$

and the output state is

$$|\Psi\rangle = e^{-iH_I(t)}|vac\rangle \simeq (1 - iH_I(t) - \frac{1}{2}H_I^2(t))|vac\rangle \tag{3.2}$$

Typically the pre-factor C, that depends on pump power, is small for realistic pump powers and the term linear in H_I, which corresponds to the generation of single pairs by SPDC, is small as compared to vacuum.

The integrals for the linear term in equation 3.2 results in a bi-photon amplitude behind the crystal given by

$$A(q_s, q_i) = C\text{sinc}(\frac{L}{2}\Delta k(q_s, q_i)) \simeq C\text{sinc}(\frac{L}{4k_p}|q_s - q_i|^2)), \tag{3.3}$$

where C a constant, $q_{s,i} = k_{\perp s,i}$ are the components of the wave vector normal to the pump propagation direction and $\Delta k(q_s, q_i)$ is the phase mismatch. In the last step we took $k_{||p} = k_{||1} + k_{||2} + k_m$ and we neglect birefringence of the crystal. The two-photon amplitude can be written in angles by making use of $k_{s,i}\theta_{s,i} = q_s = -q_i$ to yield,

$$A(\theta_s, \theta_i) = C\text{sinc}(\frac{k_{p,air}\theta_s^2 L}{4n}) \tag{3.4}$$

Equation 3.4 predicts a sinc function with distinct minima, which would result in multiple rings as in reference [11]. Instead the experimental data in figure 3.2 shows one big ring. Similar to the SHG with a pulsed pump in figure 2.3, the difference is due to the Fourier related frequency spread related to the short pump pulses. We could add this to the above equation by adding the term from the SHG equation 2.5 resulting in

$$A(\theta_s, \theta_i, \Delta\omega_s, \Delta\omega_i) = C\text{sinc}(\pi \frac{\omega_p - \omega_{p0}}{\Delta\omega_{SHG}} + \frac{k_{p,air}\theta_s^2 L}{4n}) \tag{3.5}$$

3.3 Quantitative description SPDC

In this section we present experimental results for SPDC generated with pulsed laser excitation in order to gain a better quantitative idea of the SPDC process. In particular we study the temperature dependence of the SPDC process and report the opening angle of the SPDC light in figure 3.3 and the intensity in figure 3.4 as function of crystal temperature. Figure 3.3 shows a false color plot of SPDC ring after radial integration as function of temperature. The SPDC light is filtered by a 1 nm bandpass filter at 826 nm. The radius of the ring is indicated on the vertical axis, while crystal temperature is indicated at the horizontal axis. SPDC becomes collinear when the light makes an angle of 0 mrad, at a temperature of 40.3 °C. As expected the radius of the SPDC light changes with the square root of the temperature. A fit to the data with $r = A\sqrt{1 - \frac{T}{B}}$ with T in Celsius results in $A = 64.2 \pm 0.4\ mrad$ and $B = 41.3 \pm 0.4$ °C. Here A is the radius at 0 °C and B the temperature for collinear SPDC.

Figure 3.4 shows the total intensity of the SPDC light filtered with a 1 nm bandpass filter at 826 nm as function of temperature. For temperatures below 20 °C clipping of the SPDC light by the finite numerical aperture of the setup decreases the intensity of the SPDC light. At the colinear phase-matching temperature of 41.3 °C the intensity of the SPDC light is halved. This is due to the fact that the phase-mismatch can only be positive and effectively half of the ring has disappeared.

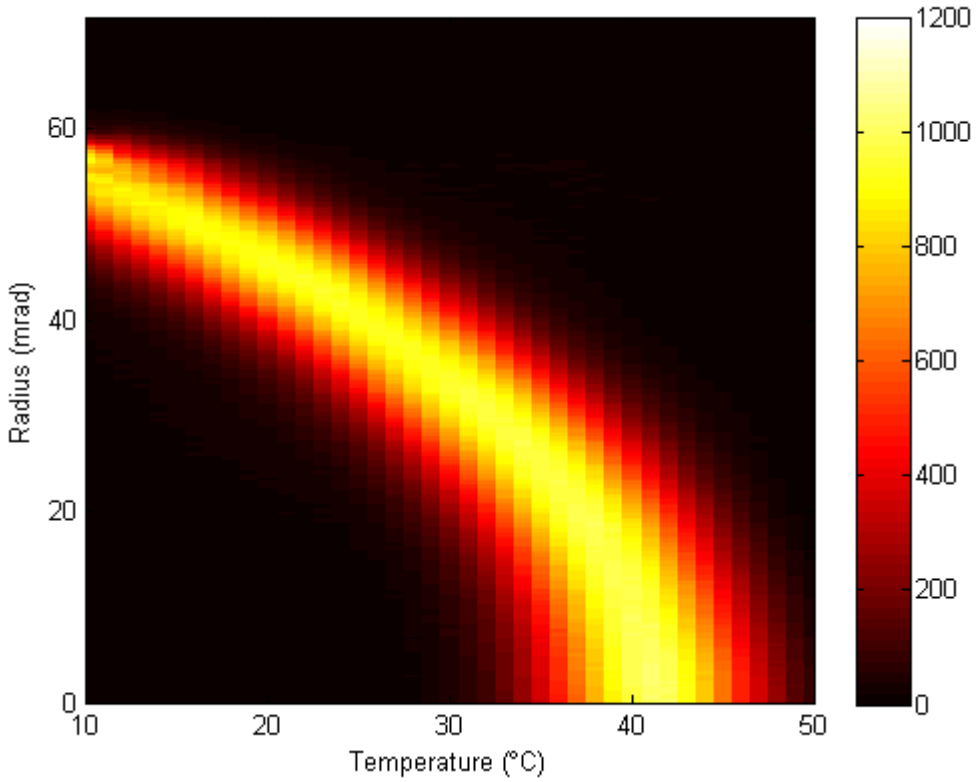

Figure 3.3: *Radially integrated intensity of the SPDC rings for a 2 mm PPKTP crystal as a function of temperature. The SPDC light is filtered by a 1 nm FWHM bandpass filter centered at 826.34 nm.*

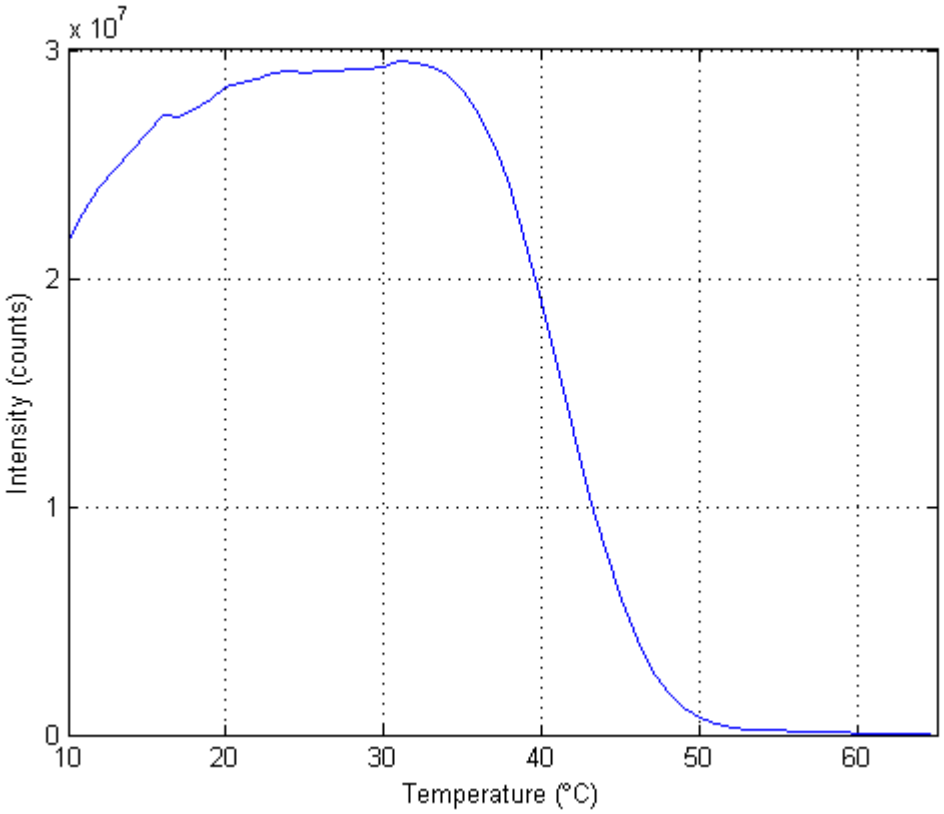

Figure 3.4: *Total intensity of the SPDC rings from a 2 nm PPKTP crystal filtered with a 1 nm bandpass filter as function of temperature. Clipping of the SPDC light by the finite numerical aperture of the setup decreases the intensity for temperatures below* 20 $^\circ C$.

Chapter 4

Spatially entangled two-photon state

4.1 What is spatial entanglement?

Spatial entanglement is a correlation of the transverse wave vector for a pair of photons. A measurement of the emission direction of an individual photon does not give extra information compared to the classical intensity measurement. However, when correlations are studied between two photons belonging to a single pair the measurement of the emission direction of the one photon determines the direction of the second photon. These photon pairs are entangled and it is not possible to write the transverse wave vector of one photon independent of the transverse wave vector of the other photon. The value of q_1 depends on q_2, and the amplitude of the two-photon state can not be written as a product of two one-photon amplitudes: $A(q_1, q_2) \neq f(q_1)g(q_2)$.

4.2 How to measure it?

Figure 4.1 shows the setup for detecting the spatial entanglement of two photons produced by SPDC. The 413 nm pulsed pump beam is focused with a $f = 500$ mm lens. The beam waist of the pump beam is calculated, from the specifications of the beam diameter exiting the laser, to be 126 μm and is located in the middle of the crystal. Two detectors are placed in the far-field

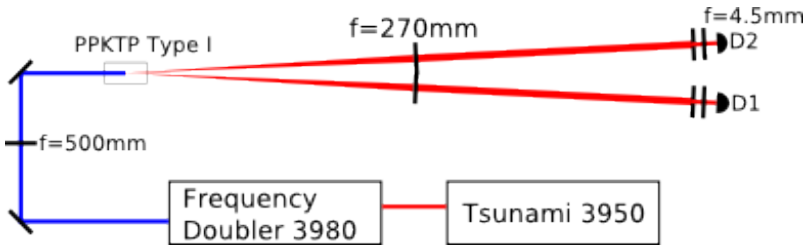

Figure 4.1: *Experimental setup used to record two-photon correlations of photon pairs generated in a spontaneous parametric down conversion process at 826nm in a Type 1 PPKTP crystal. The pump laser generating 2 ps pulses at 413 nm is focused with a f=500 mm lens in the center of the crystal. The photon pairs are collected at an angle of 50 mrad with a f=270 mm lens. In the far-field an aperture selects the spatial modes. After the aperture the light is collected into a multi mode fiber (diameter 50 μm) with a $f = 4.5$ mm lens connected to a Perkin Elmer SPCM-AQ4C single photon detector. In the upper arm, the aperture, lens and fiber are all placed on a single translation stage. The aperture size in the lower arm is 0.8 mm and the aperture size in the upper arm is 1 mm.*

at opposite sites of the far-field SPDC ring with an half opening angle of 50 mrad. A $f = 270$ mm lens in each arm is used to create the far-field image. Two apertures with diameter $d = 1$ mm selects the spatial modes. After the aperture the light is collected into a multi mode fiber (diameter 50 μm) with a $f = 4.5$ mm lens connected to a Perkin Elmer SPDC-AQ4C (500 s^{-1} dark, 45% quantum efficiency at 826 nm) single photon detector. The aperture, lens and fiber are all placed on a single translation stage. Moving this translation stage, situated in the far-field of the SPDC light will result in detecting different transverse wave vectors.

Figure 4.2 a-c) shows false-color images of the counts of detector 2, divided by 60, as a function of position in the x and y direction. Figures a, b and c corresponds to crystal temperatures of 15.8 °C, 20.4 °C and 25.75 °C respectively. In these images one can see a part of the ring of figure 3.2 that can be seen by the single photon detector. For higher temperatures the radius of the ring decreases.

Figures 4.2 d-f) show false color plots of the coincidences between detector 1 and 2 for a fixed position of detector 1 and the same crystal temperatures as in figures a-c. The coincidence peak does not move with temperature like

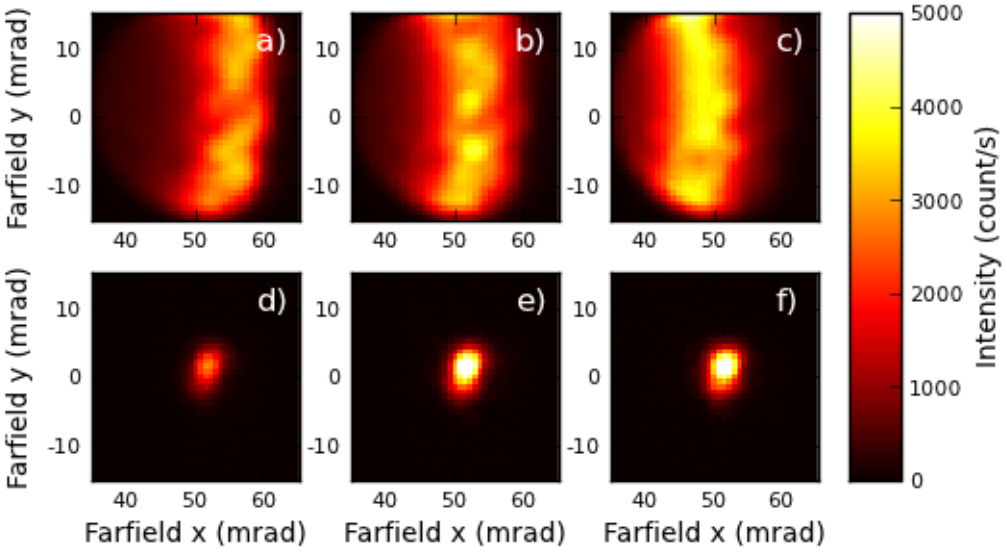

Figure 4.2: *a-c) the counts at detector 2 divided by 60, for a part of the ring. The crystal temperatures are 15.8 °C, 20.4 °C and 25.75 °C respectively. d-f the coincidence counts between detector 1 and 2 for the same temperatures. The light is filtered with a 5 nm bandpass filter.*

the singles. The position is equal to the position of the fixed detector 1 for all temperatures. This shows that selecting the transverse wave vector at detector 1 will set the wave vector at detector 2 independent of the diameter of the ring. The observed coincidences can thus be represented in terms of the difference in position on detector 1 an 2.

Figure 4.3 shows the measured singles on detector 2 and coincidences as a function of the position of the detector in the horizontal x-direction. The blue curve shows the single counts on detector 2 and the green curve is the coincidence counts between detector 1 and 2. The dashed lines are a Lorenzian and a Gaussian fit to the single and coincidence data respectively. The FWHM of these fits are $w_{singles} = 9.68 \pm 0.73$ mrad for the singles and $w_{coincidences} = 3.70 \pm 0.03$ mrad for the coincidence peak. Their ratio is $R = 2.62 \pm 0.20$ which is an indication of the number of modes as explained

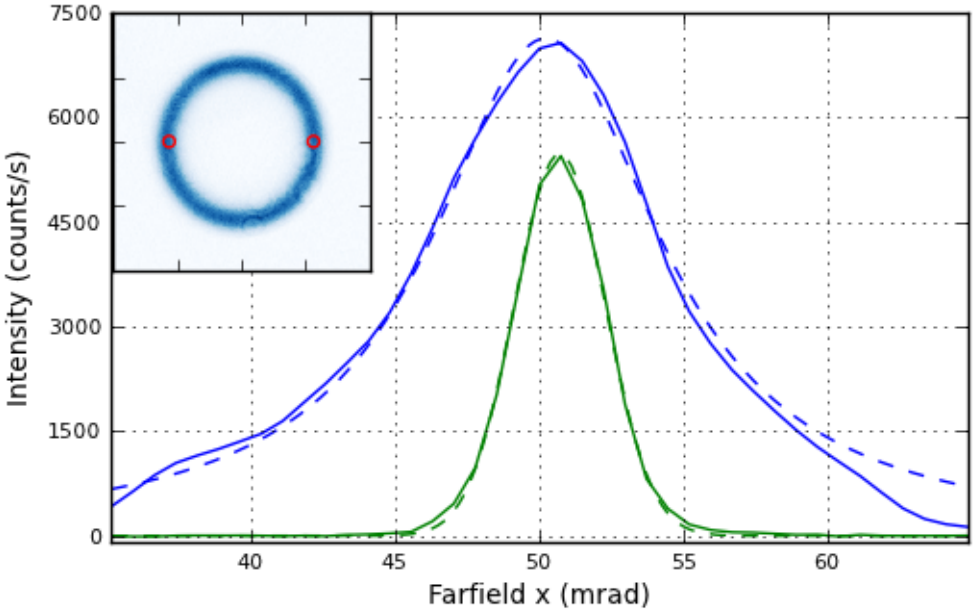

Figure 4.3: *Single count rate at detector 2 (blue line) and coincidence rate between detector 1 and 2 (green line) as a function of far-field angle in the x-direction for a 5 nm bandpass filter. Single rates are divided by a factor 30. The dashed curves are a Lorenzian and a Gaussian fit to the single and coincidence data, respectively, resulting in a FWHM of* 9.68 ± 0.73 *mrad and* 3.70 ± 0.03 *mrad. The inset shows a CCD image of the SPDC ring in the far-field filtered by a 1 nm bandpass filter. The red circles indicate the approximate position of detector 1 and 2.*

in the next section.

4.3 Number of modes

A Schmidt decomposition is a way to calculate the number of distinct eigenmodes available for an (entangled) quantum state. Law and Eberly [6] calculated the Schmidt number K for the spatial entanglement of SPDC photon pairs. They write the 2-photon field as

$$A_{focused}(q_s, q_i) \propto e^{-|q_s+q_i|^2/\sigma^2} \mathrm{sinc}(\frac{L}{4k_p}|q_s - q_i|^2). \tag{4.1}$$

Law and Eberly showed that with Gaussian-Hermite or Gaussian-Laguerre mode expansion the Schmidt number can be conveniently written as

$$K = \frac{1}{4}\left(b\sigma + \frac{1}{b\sigma}\right)^2, \tag{4.2}$$

where $b^2 = \frac{L}{4k_p}$ is the width of the phase-match function and $\sigma = \frac{2}{w_{pump}}$ is the inverse width of the pump beam. Following [13] the number of modes in the horizontal x direction results in

$$K_x = \frac{1}{2}\left(b\sigma_\perp + \frac{1}{b\sigma_\perp}\right) \tag{4.3}$$

where b and σ are now the effective inverse width and width of the sinc and pump beam respectively. This Schmidt number is an indication of the number of spatial modes.

In an experiment this number K is equal to the ratio of the measured width of the singles over the width of the coincidence peak. This can be seen by writing the width of the singles and coincidences peak in terms of σ and b. For the singles peak this gives $\sigma_{singles} = \frac{1}{2}\sqrt{\frac{1}{b^2} + \sigma^2}$ and for the coincidences peak $\sigma_{coincidences} = \frac{\sigma}{\sqrt{b^2\sigma^2+1}}$. The number of modes now becomes

$$K_x = \frac{\sigma_{singles}}{\sigma_{coincidences}}. \tag{4.4}$$

Equation 4.4 holds only if there are no filters and the pump is continuous wave. If we approximate the aperture (a spatial filter) with a Gaussian we get the FWHM as $w_{aperture} = \frac{d}{f} = 3.7$ mrad. This minimum detection width limits our detection of the coincidence peak and the ratio of the width of the coincidences and the singles should be interpreted as a lower limit for the number of modes $K_x \geq R = 2.62 \pm 0.20$. In reference [13], the effect of a spatial filter is described as an effective b given by $b_{eff} = \sqrt{b^2 + a^2/2}$.

Calculating the single and coincidence width for a non-pulsed, non-collinear, focused pump, with a factor $0.88\frac{\lambda_s}{2\pi}$ to transform the sigmas mentioned above into FWHM widths, results in $w_{singles} = 7.0$ mrad and $w_{coincidences} = 1.8$ mrad. This results in $K_x = 3.8$ spatial modes in the x-direction. The width of the coincidences seems a factor 2 under estimated and the width of the singles will be broader by the spectral width.

Chapter 5

Four-photon spatial entanglement

5.1 Introduction to four-photon state

We will now investigate the second-order process in SPDC that produces 4-photons. This second-order process can either produce 4 photons that are in a four-photon entangled state, or it can produce a double pair state.

Here the first process corresponds to stimulated emission of a second photon pair by the first spontaneous pair, while the second process corresponds to the spontaneous emission of two independent pairs. For a single spatial and temporal mode both processes have equal probability. Depending on the number of modes collected by the detector the relative amplitude of the stimulated process will be reduced. Thus, to observe the stimulated process, the number of spatial-temporal modes collected should be small.

It is essential to use a pulsed laser so that the photons are generated in a well defined time bin. The use of a CW pump generates a very large number of temporal modes, i.e., the inverse of the bandwidth of the SPDC, and reduces the visibility to nearly zero. Even in the case of a pulsed pump, the SPDC light should be filtered by a narrow bandpass filter to increase the coherence time of the SPDC light, in order to decreases the number of temporal modes.

5.2 Measurement

The setup to measure the correlations due to a four-photon state with two detectors is shown in figure 5.1. An extra beam splitter is added in the upper arm compared to the setup to measure 2-photon spatial entanglement (figure 4.1). This extra beam splitter gives the possibility to detect 2 photons in one arm. Because all photon pairs will send one photon to the lower arm and the second photon to the upper arm, coincidences between D2 and D3 probe 4 photon events. It is then sufficient to show that 2 photons in one arm are entangled for having a 4-photon entangled state.

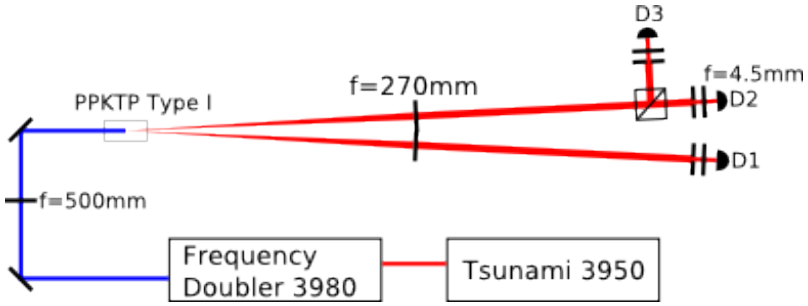

Figure 5.1: *Experimental setup used to record spatial correlations between two photons in one arm. The setup is equal to the two-photon setup figure 4.1 except that an extra beam splitter is added in the far-field of the upper arm and a copy of the translation stage with aperture, lens and fiber is placed at the second exit of the beam splitter.*

To measure the coincidences between two different pump pulses, an electronic delay is added after one of the detectors. This electronic delay delays the signal that is send from the photon counter to the coincidence counter. The range of this electronic delay is 64 ns and the minimal step size is 250 ps.

For the two detectors, D2 and D3, at the same far-field position figure 5.2 gives the coincidences as a function of delay time. The middle peak is due coincidences of pairs in the same laser pulse, while the side peaks are due to coincidences of pairs in different laser pulses.

In figure 5.3 the singles and fourfold coincidences are shown for a scan of detector 2 in the y plane at x = 50 mrad. The fourfold coincidences are taken between detector 2 and 3 where detector 3 is placed at a far-field angle

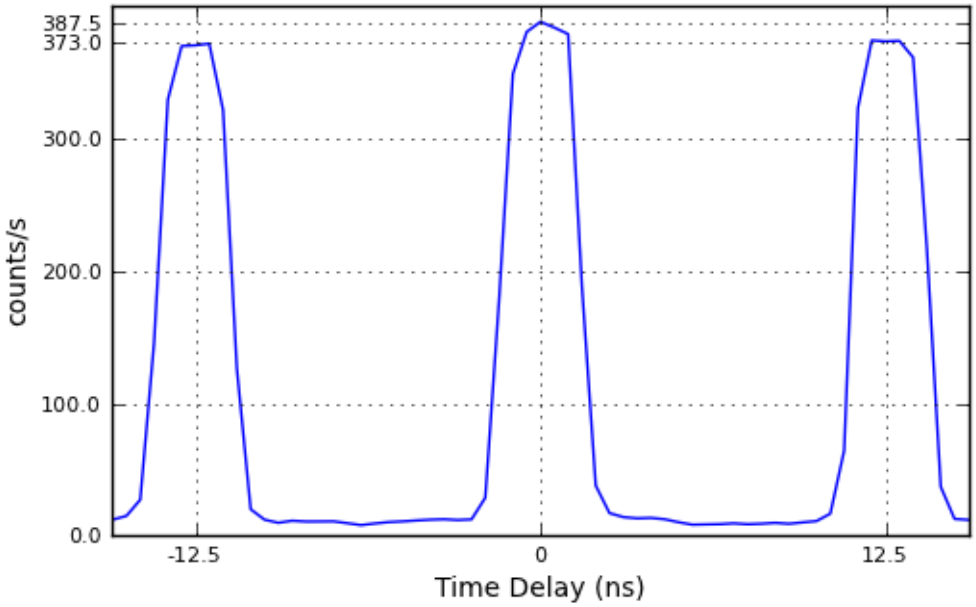

Figure 5.2: *Coincidences of the SPDC light between detector 2 and 3 filtered with a 5 nm bandpass filter and a 1 mm aperture. On the y axis, we have the delay of arrival time of the detection pulse at the coincidence counter. The difference between the peak at zero delay and the others are the fourfold coincidences.*

of 50 mrad in the x plane and at -3.7 mrad, 0 mrad and 3.7 mrad in the y-plane for the blue, red and green line respectively. The black line are the singles scaled down by a factor ten thousand.

A scan in the x-direction is shown in figure 5.4. Here detector 3 is placed at 46.3 mrad, 50 mrad and 53.7 mrad in the x plane for the blue, red and green line respectively. And detector 2 is scanned in the x plane. The singles and the middle coincidence peak are fitted by a Gaussian with FWHM 9.62 ± 0.64 mrad and 3.47 ± 0.30 mrad respectively. This values are in good agreement with the values of the 2 photon case, and the ratio is $R = 2.77 \pm 0.30$.

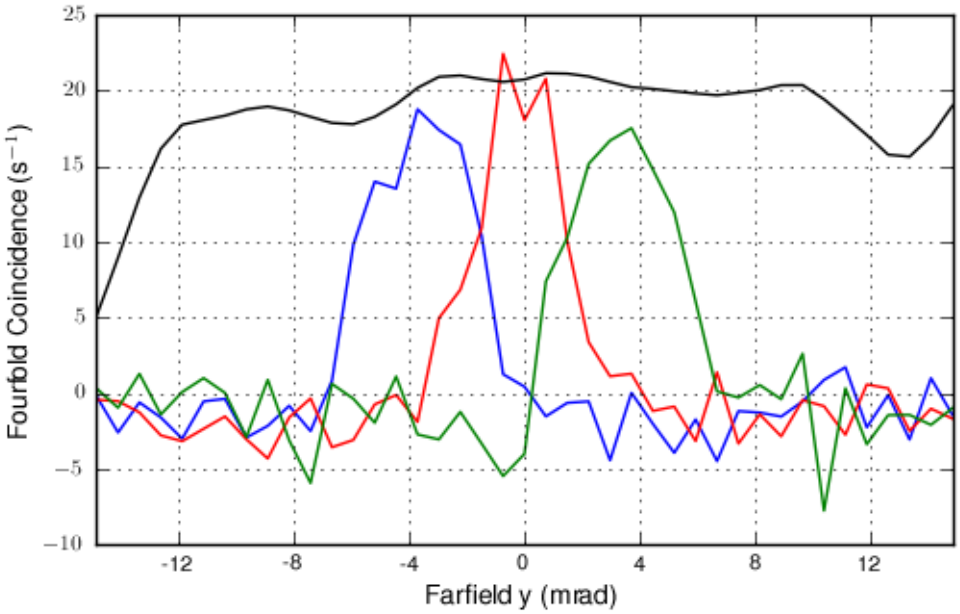

Figure 5.3: *The coincidences of detector 2 and 3 for position of detector 2. The position of detector 3 is -3.7 mrad for the blue line, 0 mrad for the red line and 3.7 mrad for the green line. In the x plane both detectors are placed at 50 mrad. The black line are the single counts at detector 2 scaled by a factor of 10 000. The light is filtered by a 5 nm bandpass filter*

5.3 Conclusions for observing 4-photon spatial entanglement

A way to calculate the ratio between the 4 photon and the 2x2 photon states is to measure the coincidences within one pulse and between two subsequent pulses. Measuring within the same pulse gives the probability for creating 4 photons P_4, while measuring between two pulses corresponds to the probability of creating two independent pairs devoted by P_2^2.

$$P_4 = \frac{P_2^2}{2}(1+\chi). \tag{5.1}$$

Here the factor 1/2 comes from the Poissonian statistics. For a single spatial mode the parameter χ is given by [12]

$$\chi = \frac{r}{(1+r^2)^{1/2}} \approx r = \frac{t_c^{ph}}{\tau} = \frac{1}{N_{frequency}}. \tag{5.2}$$

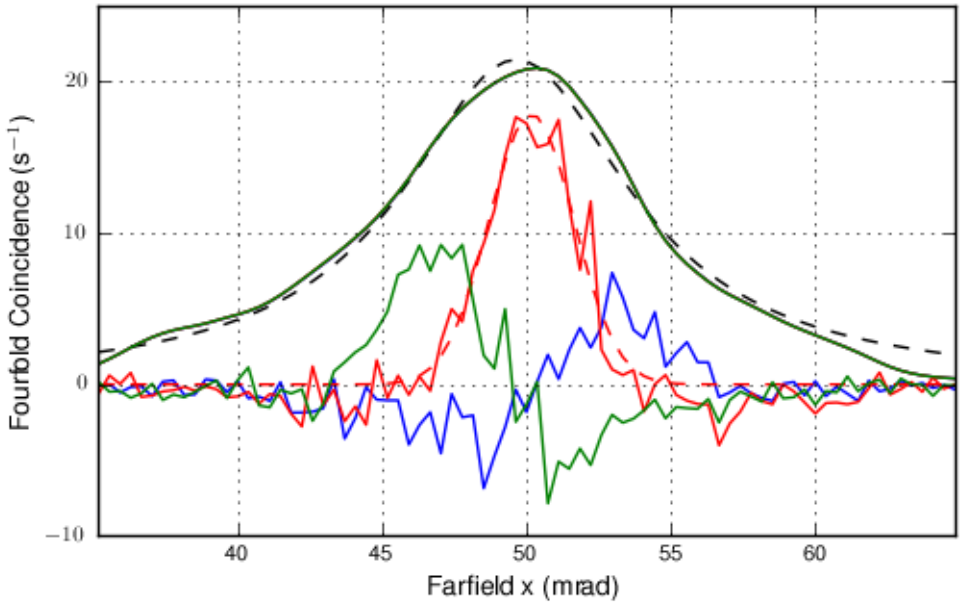

Figure 5.4: *The coincidences of detector 2 and 3 for position of detector 2. The position of detector 3 in the x plane is 46.3 mrad for the blue line, 50 mrad for the red line and 53.7 mrad for the green line. The black line are the single counts at detector 2 scaled by a factor of 10 000. The light is filtered by a 5 nm bandpass filter. The singles and middle coincidence peak are fitted with a Gaussian. The widths of the Gaussian are* 9.62 ± 0.64 *mrad and* 3.47 ± 0.30 *mrad for the singles and coincidences respectively. There ratio is* $K_x = 2.77 \pm 0.30$.

Here t_c^{ph} is the coherence length of the photons and τ the pulse length of the pump laser. The last step holds for $r << 1$. $\frac{\tau}{t_c^{ph}}$ is the number of frequency modes collected. An intuitive explanation for the value of χ is that a photon pair can be generated in N modes, while, generating two pairs in the same mode gives an enhancement of a factor 2 due the stimulated emission.

In our setup not only frequency modes but also spatial modes are generated. For each spatial mode, $\frac{\tau}{t_c^{ph}}$ frequency modes are also collected. For every two photons generated at the same mode, there are also $N-1$ photons generated in other modes. If there are multiple frequency modes as well as multiple spatial modes, the total number of modes is given by $N = N_{spatial} N_{frequency}$.

The difference in height between the center peak and the side peaks in figure 5.2 is 3.8%. This indicates that there are around 26 spatial-temporal

modes collected. A bandpass filter with a FWHM of 5 nm gives a coherence time of the photons of $t_c^{ph} = \frac{0.44\lambda^2}{c\Delta\lambda} = 0.20$ ps. For the laser pulse duration of 2 ps the number of temporal modes is $N_{frequency} = 10$, leaving 2.6 spatial modes collected simultaneously. This number of spatial modes is not the number of spatial modes generated as measured in figure 5.4, but the number of spatial modes that pass though the aperture of the detector simultaneously.

The graphs in figure 5.3 and 5.4 show small negative numbers. We currently believe this is due to contributions from higher order terms involving 6 photons. In appendix A the calculation of the 3rd order term of the SPDC process is presented. In the conclusion of this calculation the number of coincidences expected to detect in one pulse or between two pulses is presented. This difference between this two numbers gives a small negative value. This negative number depends on the total number of modes generated.

5.4 Follow-up experiments to improve the visibility

The experiments of the previous sections show only 3.8% of the 4-photons generated to be four-photon states. It should be possible to increase this number by decreasing the number of modes collected simultaneously by the detector.

In figure 5.5 the visibility of the 4 photon state as function of aperture size is shown for a 5 nm bandpass filter (red squares) and a 1 nm bandpass filter (blue circles). In contrast to the previous measurements the lens that focuses the pump beam on the crystal has a focal length of 300 mm in this measurement. The visibility here is defined as $\frac{2P_4}{P_2^2}$ and is measured by positioning detector 2 and 3 at the same position and divide the coincidences in one pulse by the coincidences between two pulses.

The results of figure 5.5 show a clear improvement in visibility between the two bandpass filters. This improvement is due to the reduction of frequency modes collected. Also the reduction of the spatial modes collected, by reducing the size of the aperture, shows a clear improvement. The numbers in the graph are not comparable with older results due to the fact that

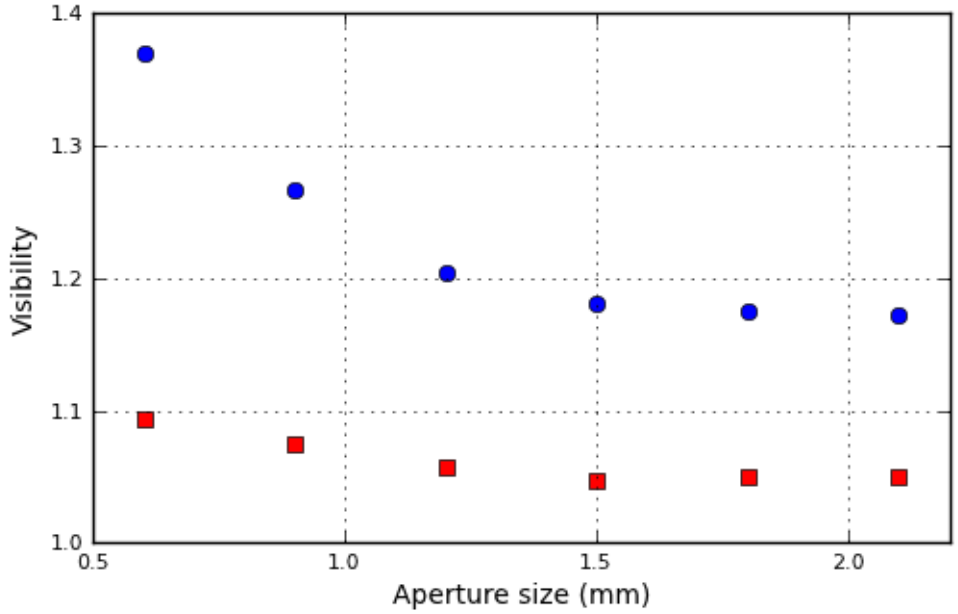

Figure 5.5: *Visibility of the 4-photon state as function of the aperture size, for a SPDC light filtered by a 5 nm bandpass filter (red squares) and filtered by a 1 nm bandpass filter (blue circles) at 826 nm center frequency and a focus lens for the pump of 300 mm. The visibility here is defined as* $\frac{2P_4}{P_2^2}$*. For aperture sizes under the 1.5 mm the visibility goes linear up. For bigger aperture sizes the aperture collects all modes and the visibility stays constant.*

the lens to focus the light in the crystal is changed. The stronger focus reduces the number of spatial modes generated and changes the typical size of a spatial modes in the far-field and thus changes the number of spatial modes collected by the aperture.

To complete the investigation of the visibility of the 4-photon states, as shown in figure 5.5, smaller apertures and lenses with smaller focal length for focusing the pump beam are needed. We expected that for smaller apertures the visibility saturates because the aperture then only selects one spatial mode. For smaller focal length of the lens in the pump beam, a higher visibility is expected at aperture sizes that collect all modes. This is due the fact that when all spatial modes are collected, the number of spatial modes collected is smaller due to small number of total spatial modes generated.

5.5 Discussion

In the first three sections of this chapter we have seen the results of 4 photon experiments. The ratio 4-photon states to 2x2 photon states in this results is very low. In section 5.4 the first experiments of improving this ratio show that the visibility can be increased from ¡4% to ¿30%. This project will continue in the lab to further optimize the visibility and number of 4-photon states generated. This can be done by minimizing the number of collected modes in the spatial and frequency domain, by using smaller apertures and narrow bandpass filters. The large increase in visibility is mostly due to the 5-fold decrease in the bandwidth of the bandpass filter.

An other effect that needs further investigation is the negative counts as shown in figure 5.3 and 5.4. As already stated in section 5.3 this effect probably depends on the number of total modes generated. When the visibility is optimized by collecting less modes this effect will get less prominent.

Appendix A

Calculation of the coincidence rates

The Hamiltonian and the state created by SPDC are given by:

$$\begin{aligned} H &= \sum_{i=1}^{N} \tilde{\kappa} \mathcal{A}^{\dagger}_{\vec{q_i}} + \text{h.c.} \\ \mathcal{A}^{\dagger}_{\vec{q_i}} &= a^{\dagger}_{\vec{q_i}} a^{\dagger}_{-\vec{q_i}} \\ |\Psi\rangle = \exp(-iH\frac{t}{\hbar})|0\rangle &\approx (1 - \frac{it}{\hbar}H - \frac{t^2}{2\hbar^2}H^2 + \frac{it^3}{6\hbar^3}H^3)|0\rangle \end{aligned} \tag{A.1}$$

The different contributions are then:

$$H|0\rangle \;=\; \tilde{\kappa} \sum_{i=1}^{N} \mathcal{A}^{\dagger}_{\vec{q_i}}|0\rangle = \tilde{\kappa} \sum_{i=1}^{N} |\vec{q_i}; -\vec{q_i}\rangle$$

The linear term creates N pairs, each in a single spatial mode.

$$
\begin{aligned}
H^2|0\rangle &= \tilde{\kappa}^2 \sum_{j=1}^{N} (\mathcal{A}^\dagger_{\vec{q_j}} + \mathcal{A}_{\vec{q_j}}) \sum_{i=1}^{N} \mathcal{A}^\dagger_{\vec{q_i}} |0\rangle = \tilde{\kappa}^2 (\sum_{j=1}^{N} \sum_{i=1}^{N} \mathcal{A}^\dagger_{\vec{q_j}} \mathcal{A}^\dagger_{\vec{q_i}} |0\rangle + N|0\rangle) \\
&= \tilde{\kappa}^2 (\sum_{i=1}^{N} \mathcal{A}^\dagger_{\vec{q_i}} \mathcal{A}^\dagger_{\vec{q_i}} |0\rangle + \sum_{j=1}^{N} \sum_{i=1, i\neq j}^{N} \mathcal{A}^\dagger_{\vec{q_j}} \mathcal{A}^\dagger_{\vec{q_i}} |0\rangle + N|0\rangle) \\
&= \tilde{\kappa}^2 (\sum_{i=1}^{N} 2|\vec{q_i}; -\vec{q_i}\rangle \otimes |\vec{q_i}; -\vec{q_i}\rangle + \sum_{j=1}^{N} \sum_{i=1, i\neq j}^{N} |\vec{q_j}; -\vec{q_j}\rangle \otimes |\vec{q_i}; -\vec{q_i}\rangle + N|0\rangle)
\end{aligned}
$$

The quadratic term creates $2N$ double pairs in the same mode, and $N(N-1)$ pairs with the two photons in different spatial modes. This last term corresponds to the total number of possibilities to distribute two photons over N bins, given that no two photons should occupy the same mode. There are N ways to put two photons in the same mode. The extra factor 2 in that term arises from the creation operators that create two photons in the same mode. This factor two is exactly the term that gives rise to stimulated emission! It is easier to create a second photon in the same mode than what one would expect based on a statistical argument.

$$
\begin{aligned}
H^3|0\rangle &= \tilde{\kappa}^3 \sum_{k=1}^{N} (\mathcal{A}^\dagger_{\vec{q_k}} + \mathcal{A}_{\vec{q_k}}) (\sum_{j=1}^{N} \sum_{i=1}^{N} \mathcal{A}^\dagger_{\vec{q_j}} \mathcal{A}^\dagger_{\vec{q_i}} |0\rangle + N|0\rangle) \\
&= \tilde{\kappa}^3 (N \sum_{i=1}^{N} \mathcal{A}^\dagger_{\vec{q_i}} |0\rangle + \sum_{k=1}^{N} \sum_{j=1}^{N} \sum_{i=1}^{N} \mathcal{A}^\dagger_{\vec{q_k}} \mathcal{A}^\dagger_{\vec{q_j}} \mathcal{A}^\dagger_{\vec{q_i}} |0\rangle + \sum_{k=1}^{N} \sum_{j=1}^{N} \sum_{i=1}^{N} \mathcal{A}_{\vec{q_k}} \mathcal{A}^\dagger_{\vec{q_j}} \mathcal{A}^\dagger_{\vec{q_i}} |0\rangle) \\
&= \tilde{\kappa}^3 (N \sum_{i=1}^{N} \mathcal{A}^\dagger_{\vec{q_i}} |0\rangle + \sum_{i=1}^{N} (\mathcal{A}^\dagger_{\vec{q_i}})^3 |0\rangle + \sum_{j=1}^{N} \sum_{i=1, i\neq j}^{N} \mathcal{A}^\dagger_{\vec{q_j}} (\mathcal{A}^\dagger_{\vec{q_i}})^2 |0\rangle + \\
&\quad \sum_{k=1}^{N} \sum_{j=1, j\neq k}^{N} \sum_{i=1, i\neq j\neq k}^{N} \mathcal{A}^\dagger_{\vec{q_k}} \mathcal{A}^\dagger_{\vec{q_j}} \mathcal{A}^\dagger_{\vec{q_i}} |0\rangle + \sum_{i=1}^{N} \mathcal{A}_{\vec{q_i}} (\mathcal{A}^\dagger_{\vec{q_i}})^2 |0\rangle + \\
&\quad \sum_{j=1}^{N} \sum_{i=1, i\neq j}^{N} \mathcal{A}_{\vec{q_j}} \mathcal{A}^\dagger_{\vec{q_j}} \mathcal{A}^\dagger_{\vec{q_i}} |0\rangle + \sum_{j=1}^{N} \sum_{i=1, i\neq j}^{N} \mathcal{A}_{\vec{q_j}} \mathcal{A}^\dagger_{\vec{q_i}} \mathcal{A}^\dagger_{\vec{q_j}} |0\rangle) \\
&= \tilde{\kappa}^3 (N \sum_{i=1}^{N} \mathcal{A}^\dagger_{\vec{q_i}} |0\rangle + \sum_{i=1}^{N} (\mathcal{A}^\dagger_{\vec{q_i}})^3 |0\rangle + \sum_{j=1}^{N} \sum_{i=1, i\neq j}^{N} \mathcal{A}^\dagger_{\vec{q_j}} (\mathcal{A}^\dagger_{\vec{q_i}})^2 |0\rangle + \\
&\quad \sum_{k=1}^{N} \sum_{j=1, j\neq k}^{N} \sum_{i=1, i\neq j\neq k}^{N} \mathcal{A}^\dagger_{\vec{q_k}} \mathcal{A}^\dagger_{\vec{q_j}} \mathcal{A}^\dagger_{\vec{q_i}} |0\rangle + 4 \sum_{i=1}^{N} \mathcal{A}^\dagger_{\vec{q_i}} |0\rangle + 2(N-1) \sum_{i=1}^{N} \mathcal{A}^\dagger_{\vec{q_i}} |0\rangle) \\
&= \tilde{\kappa}^3 ((3N+2) \sum_{i=1}^{N} \mathcal{A}^\dagger_{\vec{q_i}} |0\rangle + \sum_{i=1}^{N} (\mathcal{A}^\dagger_{\vec{q_i}})^3 |0\rangle + \sum_{j=1}^{N} \sum_{i=1, i\neq j}^{N} \mathcal{A}^\dagger_{\vec{q_j}} (\mathcal{A}^\dagger_{\vec{q_i}})^2 |0\rangle + \\
&\quad \sum_{k=1}^{N} \sum_{j=1, j\neq k}^{N} \sum_{i=1, i\neq j\neq k}^{N} \mathcal{A}^\dagger_{\vec{q_k}} \mathcal{A}^\dagger_{\vec{q_j}} \mathcal{A}^\dagger_{\vec{q_i}} |0\rangle) \\
&= \tilde{\kappa}^3 ((3N+2) \sum_{i=1}^{N} |\vec{q_i}; -\vec{q_i}\rangle + 6 \sum_{i=1}^{N} |\vec{q_i}; -\vec{q_i}\rangle \otimes |\vec{q_i}; -\vec{q_i}\rangle \otimes |\vec{q_i}; -\vec{q_i}\rangle + \\
&\quad 2 \sum_{j=1}^{N} \sum_{i=1, i\neq j}^{N} |\vec{q_j}; -\vec{q_j}\rangle \otimes |\vec{q_i}; -\vec{q_i}\rangle \otimes |\vec{q_i}; -\vec{q_i}\rangle + \\
&\quad \sum_{k=1}^{N} \sum_{j=1, j\neq k}^{N} \sum_{i=1, i\neq j\neq k}^{N} |\vec{q_k}; -\vec{q_k}\rangle \otimes |\vec{q_j}; -\vec{q_j}\rangle \otimes |\vec{q_i}; -\vec{q_i}\rangle)
\end{aligned}
$$

The H^3 term can be interpreted in a similar way. There are $N(N-1)(N-2)$ ways to distribute 3 photons over N modes if each of the photons is in a different mode. There are $N(N-1)$ ways to distribute 3 photons over

N modes if 2 photons need to be in the same mode, while the third photon is in a different mode. This term gets an extra factor 2 from the creation operators that create two photons in the same mode. Similarly, there are N ways to put 3 photons all in the same mode and the creation operators give an extra factor $(\sqrt{3!})^2 = 6$ to this term. The $(3N+2)N$ single photon terms are due to combinations of a single annihilation operator and a product of two creation operators.

To understand the states created after a photon detection in one of the arms of the SPDC setup a projection $a^\dagger_{\vec{q_1}}|0\rangle\langle 0|a_{\vec{q_1}}|\Psi\rangle = |\vec{q_1};\rangle\langle\vec{q_1};||\Psi\rangle$ should be calculated. In this case the photon is detected in mode 1. An expression $\frac{1}{\sqrt{2}}|\vec{q_1};\rangle \otimes |\vec{q_2};\rangle\langle\vec{q_1};| \otimes \langle\vec{q_2};|\frac{1}{\sqrt{2}}|\Psi\rangle$ then gives the state after a coincidence detection event of a photon in mode 1 and a photon in mode 2 and $\frac{\sqrt{2}}{\sqrt{2}}|\vec{q_1};\rangle \otimes |\vec{q_1};\rangle\langle\vec{q_1};| \otimes \langle\vec{q_1};|\frac{\sqrt{2}}{\sqrt{2}}|\Psi\rangle$ gives the state after a coincidence detection of 2 photons in mode 1.

$$\langle\vec{q_1};||\Psi\rangle = -\frac{it}{\hbar}\langle\vec{q_1};|H|0\rangle - \frac{t^2}{2\hbar^2}\langle\vec{q_1};|H^2|0\rangle + \frac{it^3}{6\hbar}\langle\vec{q_1};|H^3|0\rangle$$

$$\begin{aligned}
\langle\vec{q_1};|H|0\rangle &= \tilde{\kappa} \\
\langle\vec{q_1};|H^2|0\rangle &= \tilde{\kappa}^2(2|\vec{q_1};-\vec{q}_1\rangle + 2\sum_{i=2}^{N}|\vec{q_i};-\vec{q}_i\rangle) \\
\langle\vec{q_1};|H^3|0\rangle &= \tilde{\kappa^3}((3N+2) + 6|\vec{q_1};-\vec{q}_1\rangle \otimes |\vec{q_1};-\vec{q}_1\rangle + 2\sum_{i=2}^{N}|\vec{q_i};-\vec{q}_i\rangle \otimes |\vec{q_1};-\vec{q}_1\rangle \\
&\quad +2\sum_{i=2}^{N}|\vec{q_i};-\vec{q}_i\rangle \otimes |\vec{q_i};-\vec{q}_i\rangle + \sum_{j=2}^{N}\sum_{i=2,i\neq j}^{N}|\vec{q_j};-\vec{q}_j\rangle \otimes |\vec{q_i};-\vec{q}_i\rangle)
\end{aligned}$$

Coincidence detection, same spatial mode

$$
\begin{aligned}
\langle\vec{q_1};|\otimes\langle\vec{q_1};|H|0\rangle &= 0 \\
\langle\vec{q_1};|\otimes\langle\vec{q_1};|H^2|0\rangle &= \sqrt{2}\cdot 2\tilde{\kappa}^2 \\
\langle\vec{q_1};|\otimes\langle\vec{q_1};|H^3|0\rangle &= \sqrt{2}\cdot 6\tilde{\kappa}^3|\vec{q_1};-\vec{q}_1\rangle + \sqrt{2}\cdot 2\tilde{\kappa}^3\sum_{i=2}^{N}|\vec{q_i};-\vec{q}_i\rangle \\
&= 4\sqrt{2}\tilde{\kappa}^3|\vec{q_1};-\vec{q}_1\rangle + 2\sqrt{2}\tilde{\kappa}^3\sum_{i=1}^{N}|\vec{q_i};-\vec{q}_i\rangle
\end{aligned}
$$

Coincidence detection, different spatial mode

$$
\begin{aligned}
\langle\vec{q_1};|\otimes\langle\vec{q_2};|H|0\rangle &= 0 \\
\langle\vec{q_1};|\otimes\langle\vec{q_2};|H^2|0\rangle &= 2\tilde{\kappa}^2 \\
\langle\vec{q_1};|\otimes\langle\vec{q_2};|H^3|0\rangle &= 2\tilde{\kappa}^3|\vec{q_1};-\vec{q}_1\rangle + 2\tilde{\kappa}^3|\vec{q_2};-\vec{q}_2\rangle + \tilde{\kappa}^3\sum_{i=3}^{N}|\vec{q_i};-\vec{q}_i\rangle \\
&= 2\tilde{\kappa}^3\sum_{i=1}^{N}|\vec{q_i};-\vec{q}_i\rangle - \tilde{\kappa}^3\sum_{i=3}^{N}|\vec{q_i};-\vec{q}_i\rangle
\end{aligned}
$$

With the above, it is relatively straight forward to analyze the experimental situation where we subtract the coincidences measured between two different pulses from coincidences measured in the same pulse. The relevant state for these conditions is:

$$
\begin{aligned}
|\Psi_{0\ ns}\rangle\otimes|\Psi_{12\ ns}\rangle &\approx (1-\frac{it}{\hbar}H_{0\ ns}-\frac{t^2}{2\hbar^2}H^2_{0\ ns})\otimes(1-\frac{it}{\hbar}H_{12\ ns}-\frac{t^2}{2\hbar^2}H^2_{12\ ns})|0\rangle \\
&\approx 1\otimes 1|0\rangle - \frac{it}{\hbar}H_{0\ ns}\otimes 1|0\rangle - \frac{it}{\hbar}1\otimes H_{12\ ns}|0\rangle - \\
&\quad \frac{t^2}{2\hbar^2}1\otimes H^2_{12\ ns}|0\rangle - \frac{t^2}{2\hbar^2}H^2_{0\ ns}\otimes 1|0\rangle - \frac{t^2}{\hbar^2}H_{0\ ns}\otimes H_{12\ ns}|0\rangle + \\
&\quad \frac{it^3}{2\hbar^3}H^2_{0\ ns}\otimes H_{12\ ns}|0\rangle + \frac{it^3}{2\hbar^3}H_{0\ ns}\otimes H^2_{12\ ns}|0\rangle + \frac{t^4}{4\hbar^4}H^2_{0\ ns}\otimes H^2_{12\ ns}|0\rangle
\end{aligned}
$$

The relevant part of the wavefunction for coincidence detection between different pulses is

$$-\frac{t^2}{\hbar^2}H_{0\ ns}\otimes H_{12\ ns}|0\rangle+\frac{it^3}{2\hbar^3}H_{0\ ns}^2\otimes H_{12\ ns}|0\rangle+\frac{it^3}{2\hbar^3}H_{0\ ns}\otimes H_{12\ ns}^2|0\rangle$$

For the measurement we use small q to indicate a measurement at $t=0$ ns and capital Q to indicate a measurement at a delay of 12 ns. The simplest and most likely process to occur is to create a coincidence between single pairs in consecutive pulses.

$$\begin{aligned}\langle\vec{q_1};|\otimes\langle\vec{Q_1};|H_{0ns}\otimes H_{12ns}|0\rangle &= \\ \langle\vec{q_1};|H_{0ns}|0\rangle\otimes\langle\vec{Q_1};|H_{12ns}|0\rangle &= \tilde{\kappa}^2\end{aligned}$$

Similarly, the higher order terms give

$$\begin{aligned}\langle\vec{q_1}|H_{0ns}^2|0\rangle\otimes\langle\vec{Q_1};|H_{12ns}|0\rangle &= \\ (2\tilde{\kappa}^2|\vec{q_1};-\vec{q_1}\rangle+2\tilde{\kappa}^2\sum_{i=2}^{N}|\vec{q_i};-\vec{q_i}\rangle)\tilde{\kappa} &= \\ 2\tilde{\kappa}^3\sum_{i=1}^{N}|\vec{q_i};-\vec{q_i}\rangle\end{aligned}$$

and

$$\begin{aligned}\langle\vec{q_1};|H_{0ns}|0\rangle\otimes\langle\vec{Q_1};|H_{12ns}^2|0\rangle &= \\ (2\tilde{\kappa}^2|\vec{Q_1};-\vec{Q_1}\rangle+2\tilde{\kappa}^2\sum_{i=2}^{N}|\vec{Q_i};-\vec{Q_i}\rangle)\tilde{\kappa} &= \\ 2\tilde{\kappa}^3\sum_{i=1}^{N}|\vec{Q_i};-\vec{Q_i}\rangle\end{aligned}$$

The probability to detect one photon pair is

$$\|\langle\vec{q_1};||\Psi_{0\ ns}\rangle\|^2=\left\|-\frac{i\tilde{\kappa}t}{\hbar}\right\|^2=\frac{\tilde{\kappa}^2t^2}{\hbar^2}=P_2$$

The relevant projections up to the second order finally give

$$\begin{aligned}
\langle\vec{q_1};|\otimes\langle\vec{q_1};||\Psi_{0\ ns}\rangle\otimes|\Psi_{12\ ns}\rangle &= -\frac{\sqrt{2}}{\sqrt{2}}\cdot 2\frac{\tilde{\kappa}^2t^2}{2\hbar^2}\\
\langle\vec{q_1};|\otimes\langle\vec{q_2};||\Psi_{0\ ns}\rangle\otimes|\Psi_{12\ ns}\rangle &= -\frac{1}{\sqrt{2}}2\frac{\tilde{\kappa}^2t^2}{2\hbar^2}\\
\langle\vec{q_1};|\otimes\langle\vec{Q_1};||\Psi_{0\ ns}\rangle\otimes|\Psi_{12\ ns}\rangle &= -\frac{1}{\sqrt{2}}\frac{\tilde{\kappa}^2t^2}{\hbar^2}
\end{aligned}$$

now the probabilities are

$$\begin{aligned}
\|\langle\vec{q_1};|\otimes\langle\vec{q_1};||\Psi_{0\ ns}\rangle\otimes|\Psi_{12\ ns}\rangle\|^2 &= \frac{\tilde{\kappa}^4t^4}{\hbar^4}=2\frac{P_2^2}{2}\\
\|\langle\vec{q_1};|\otimes\langle\vec{q_2};||\Psi_{0\ ns}\rangle\otimes|\Psi_{12\ ns}\rangle\|^2 &= \frac{1}{2}\frac{\tilde{\kappa}^4t^4}{\hbar^4}=\frac{P_2^2}{2}\\
\left\|\langle\vec{q_1};|\otimes\langle\vec{Q_1};||\Psi_{0\ ns}\rangle\otimes|\Psi_{12\ ns}\rangle\right\|^2 &= \frac{1}{2}\frac{\tilde{\kappa}^4t^4}{\hbar^4}=\frac{P_2^2}{2}
\end{aligned}$$

The relevant projections finally give

$$\begin{aligned}
\langle\vec{q_1};|\otimes\langle\vec{q_1};||\Psi_{0\ ns}\rangle\otimes|\Psi_{12\ ns}\rangle &= \frac{1}{\sqrt{2}}\left(-\sqrt{2}\cdot 2\frac{\tilde{\kappa}^2t^2}{2\hbar^2}+4\sqrt{2}\frac{i\tilde{\kappa}^3t^3}{6\hbar^3}|\vec{q_1};-\vec{q}_1\rangle+\right.\\
&\qquad \left.2\sqrt{2}\frac{i\tilde{\kappa}^3t^3}{6\hbar^3}\sum_{i=1}^{N}|\vec{q_i};-\vec{q}_i\rangle\right)\\
\langle\vec{q_1};|\otimes\langle\vec{q_2};||\Psi_{0\ ns}\rangle\otimes|\Psi_{12\ ns}\rangle &= \frac{1}{\sqrt{2}}\left(-2\frac{\tilde{\kappa}^2t^2}{2\hbar^2}+2\frac{i\tilde{\kappa}^3t^3}{6\hbar^3}\sum_{i=1}^{N}|\vec{q_i};-\vec{q}_i\rangle-\frac{i\tilde{\kappa}^3t^3}{6\hbar^3}\sum_{i=3}^{N}|\vec{q_i};-\vec{q}_i\rangle\right)\\
\langle\vec{q_1};|\otimes\langle\vec{Q_1};||\Psi_{0\ ns}\rangle\otimes|\Psi_{12\ ns}\rangle &= \frac{1}{\sqrt{2}}\left(-\frac{\tilde{\kappa}^2t^2}{\hbar^2}+2\frac{i\tilde{\kappa}^3t^3}{2\hbar^3}\sum_{i=1}^{N}|\vec{q_i};-\vec{q}_i\rangle+2\frac{i\tilde{\kappa}^3t^3}{2\hbar^3}\sum_{i=1}^{N}|\vec{Q_i};-\vec{Q}_i\rangle\right)
\end{aligned}$$

now the probabilities are

$$\begin{aligned}
\|\langle\vec{q_1};| \otimes \langle\vec{q_1};||\Psi_{0\ ns}\rangle \otimes |\Psi_{12\ ns}\rangle\|^2 &= \frac{\tilde{\kappa}^4 t^4}{\hbar^4} + \frac{4\tilde{\kappa}^6 t^6}{9\hbar^6} + \frac{N\tilde{\kappa}^6 t^6}{9\hbar^6} + \frac{4\tilde{\kappa}^6 t^6}{9\hbar^6} \\
&= 2\frac{P_2^2}{2} + \frac{(8+N)P_2^3}{9} \\
\|\langle\vec{q_1};| \otimes \langle\vec{q_2};||\Psi_{0\ ns}\rangle \otimes |\Psi_{12\ ns}\rangle\|^2 &= \frac{1}{2}\frac{\tilde{\kappa}^4 t^4}{\hbar^4} + \frac{N\tilde{\kappa}^6 t^6}{18\hbar^6} + \frac{(N-2)\tilde{\kappa}^6 t^6}{72\hbar^6} - \frac{(N-2)\tilde{\kappa}^6 t^6}{18\hbar^6} \\
&= \frac{P_2^2}{2} + \frac{NP_2^3}{18} - \frac{3(N-2)P_2^3}{4} \\
\left\|\langle\vec{q_1};| \otimes \langle\vec{Q_1};||\Psi_{0\ ns}\rangle \otimes |\Psi_{12\ ns}\rangle\right\|^2 &= \frac{1}{2}\frac{\tilde{\kappa}^4 t^4}{\hbar^4} + \frac{N\tilde{\kappa}^6 t^6}{2\hbar^6} + \frac{N\tilde{\kappa}^6 t^6}{2\hbar^6} \\
&= \frac{P_2^2}{2} + NP_2^3
\end{aligned}$$

Because these are amplitudes, the various coefficients need to be squared in order to get coincidence rates. Substracting the last formular from the one above it gives a negative value in the P_2^3 term. This term could be one of the explanations that we get negative values in our experiments. This term depents on N, the total number of modes generated.

Bibliography

[1] Robert W. Boyd. *Nonlinear Optics*. Elsevier, 2003.

[2] Shai Emanueli and Ady Arie. Temperature-dependent dispersion equations for ktiopo4 and ktioaso4. *Appl. Opt.*, 42(33):6661–6665, Nov 2003. Refractive Index.

[3] Sonja Franke-Arnold, Stephen M. Barnett, Miles J. Padgett, and L. Allen. Two-photon entanglement of orbital angular momentum states. *Phys. Rev. A*, 65(3):033823, Feb 2002.

[4] Timothy E. Keller and Morton H. Rubin. Theory of two-photon entanglement for spontaneous parametric down-conversion driven by a narrow pump pulse. *Phys. Rev. A*, 56(2):1534–1541, Aug 1997.

[5] Friedrich Konig and Franco N. C. Wong. Extended phase matching of second-harmonic generation in periodically poled ktiopo[sub 4] with zero group-velocity mismatch. *Applied Physics Letters*, 84(10):1644–1646, 2004. EPM.

[6] C. K. Law and J. H. Eberly. Analysis and interpretation of high transverse entanglement in optical parametric down conversion. *Phys. Rev. Lett.*, 92(12):127903, Mar 2004.

[7] Y. Liu and J.-C. Diels. Group-Velocity Matched Femtosecond Parametric Oscillation by Noncollinear Quasi-Phase Matching. *IEEE Journal of Quantum Electronics*, 42:760–764, August 2006. GVM.

[8] Yu. M. Mikhailova, P. A. Volkov, and M. V. Fedorov. Biphoton wave packets in parametric down-conversion: Spectral and temporal structure and degree of entanglement. *Phys. Rev. A*, 78(6):062327, Dec 2008.

[9] Z. Y. Ou. *Multi-Photon Quantum Interference*. Springer, 2007.

[10] Z. Y. Ou, J.-K. Rhee, and L. J. Wang. Photon bunching and multiphoton interference in parametric down-conversion. *Phys. Rev. A*, 60(1):593–604, Jul 1999.

[11] W. H. Peeters and M. P. van Exter. Optical characterization ofperiodically-poled ktiopo4. *Opt. Express*, 16(10):7344–7360, May 2008. Peeters.

[12] Hugues De Riedmatten, Valerio Scarani, Ivan Marcikic, Antonio Acn, Wolfgang Tittel, Hugo Zbinden, and Nicolas Gisin. Two independent photon pairs versus four-photon entangled states in parametric down conversion. *Journal of Modern Optics*, 51(11):1637–1649, 2004. Coherence Time.

[13] M. P. van Exter, A. Aiello, S. S. R. Oemrawsingh, G. Nienhuis, and J. P. Woerdman. Effect of spatial filtering on the schmidt decomposition of entangled photons. *Phys. Rev. A*, 74(1):012309, Jul 2006.